Chiral quantum optics in broken-symmetry and topological photonic crystal waveguides

Nils Valentin Hauff ©, Hanna Le Jeannic ©,[*] and Peter Lodahl
Center for Hybrid Quantum Networks (Hy-Q), Niels Bohr Institute,
University of Copenhagen, Blegdamsvej 17, DK-2100 Copenhagen, Denmark

Stephen Hughes ©
Centre for Nanophotonics, Department of Physics, Engineering Physics & Astronomy, 64 Bader Lane,
Queen's University, Kingston, Ontario, Canada K7L 3N6

Nir Rotenberg ©
Center for Hybrid Quantum Networks (Hy-Q), Niels Bohr Institute,
University of Copenhagen, Blegdamsvej 17, DK-2100 Copenhagen,
Denmark and Centre for Nanophotonics, Department of Physics,
Engineering Physics & Astronomy, 64 Bader Lane, Queen's University, Kingston, Ontario, Canada K7L 3N6

On-chip chiral quantum light-matter interfaces, which support directional interactions, provide a promising platform for efficient spin-photon coupling, nonreciprocal photonic elements, and quantum logic architectures. We present full-wave three-dimensional calculations to quantify the performance of conventional and topological photonic crystal waveguides as chiral emitter-photon interfaces. Specifically, the ability of these structures to support and enhance directional interactions while suppressing subsequent backscattering losses is quantified. Broken symmetry waveguides, such as the nontopological glide-plane waveguide and topological bearded interface waveguide are found to act as efficient chiral interfaces, with the topological waveguide modes allowing for operation at significantly higher Purcell enhancement factors. Finally, although all structures suffer from backscattering losses due to fabrication imperfections, these are found to be smaller at high enhancement factors for the topological waveguide. These reduced losses occur because the optical mode is pushed away from the air-dielectric interfaces where scattering occurs, and not because of any topological protection. These results are important to the understanding of light-matter interactions in topological photonic crystal and design of efficient, on-chip chiral quantum devices.

I. INTRODUCTION

Chiral light-matter interactions are directional, enabling nonreciprocal devices and circuits, including unidirectional single-photon emission. This directionality arises from the interaction of elliptical dipoles with finely structured light fields of nanophotonic systems, such as plasmonic surfaces [1,2], nanowaveguides [3,4], resonators [5,6], and photonic-crystal waveguides (PhCWs) [7–9], using either classical or quantum light sources [10]. Chiral light-matter interactions enable nonreciprocal devices, such as optical isolators [8], circulators [11–13], and quantum gates [14,15], and, in waveguides, are the basis for several protocols for quantum networks [16].

Recently, a new class of topologically engineered PhCWs have been proposed and demonstrated [17–23], generating considerable excitement within the quantum optics community [24–28]. In analogy to edge modes of electronic topological insulators [29,30], the guided modes of topological PhCWs have been identified as both *chiral* [20,28,31] and resistant to backscattering in 60 degree bends [24,25,32–34]. Light propagation in all-dielectric media is described by Maxwell's equations obeying time-reversal symmetry (TRS) demanding that the complex electric field in the forward direction is the complex conjugate of the electric field in the backward direction. Light scattering from inhomogeneities (classical or quantum) alters the flow of light. In a one-dimensional waveguide, the condition referred to as chiral interaction corresponds to forward and backward propagating modes scattering with different strengths from the same (elliptically polarized) dipole. In this situation, a radiating dipole will be directional, which is referred to as chiral emission. Chiral single-photon emission has been demonstrated in topological PhCWs [24–26]. However, only few works have considered scattering losses beyond 60 degree bends that constitute inherent symmetry directions of the structure [32,35–37]. Potentially topological waveguides could

---

*Present address: Laboratoire Photonique Numérique et Nanoscience, Université de Bordeaux, Institut d'Optique, CNRS, UMR 5298, 33400 Talence, France.

have increased robustness toward backscattering loss from inherent fabrication imperfections in real devices. This could be of technological importance in quantum photonic devices where inherent backscattering leads to Anderson localization of light [38–40] thus limiting the operation length of the devices. Disorder-induced scattering also places a limit on device length for exploiting nonlinear effects in slow light PhCWs [41,42].

In this work, we use full vectorial three-dimensional finite-element simulations and rigorous scattering theory to explore how well different photonic crystal waveguides (Sec. II), and more specifically their guided modes (Sec. III), can act as quantum chiral-light matter interfaces (Sec. IV). We find that topological waveguides can be favorable compared to standard line-defect (W1) and even glide-plane waveguides [43] (GPWs) as they enable near-unity directionality at higher Purcell factors and lower propagation losses (Sec. V). We stress that the differences in loss performance arise from variations of the electric field distribution rather than the topological nature of the edge state modes, here based on the quantum valley-Hall effect [18]. This is because valley-Hall topological photonic waveguides do not break TRS, and hence the back-propagating mode is always available, in contrast with edge modes of topological electronic insulators. Finally, we show that topological waveguides, despite this lack of topological protection [44], can outperform conventional photonic crystal waveguides for the realization of integrated nonreciprocal single-photon devices for constructing of scalable complex quantum circuits and networks [45] (Sec. VI).

II. PHOTONIC CRYSTAL WAVEGUIDES AS QUANTUM CHIRAL INTERFACES

An ideal chiral interface for quantum light-matter interactions, such as the one shown in Fig. 1, is characterized by several properties. First and foremost, emission or scattering of photons by a quantum emitter (QE) into the counter-propagating modes left (L) or right (R) should be highly asymmetric with decay rates $\gamma_L \gg \gamma_R$, or vice versa. This directionality occurs when the overlap of circular (or elliptical) transition dipoles with the two counter-propagating modes differs, and is quantified by

$$D = \frac{\gamma_L - \gamma_R}{\gamma_L + \gamma_R}. \tag{1}$$

Below, we show how this directionality factor can be calculated for any electric field profile.

Second, an efficient quantum light-matter interface typically enhances photonic interactions and minimizes subsequent losses as photons solely propagate to and from the emitter. Emission enhancement into a selected, guided mode is quantified by the Purcell Factor F [46], which for PhCWs scales linearly with the group index n_g [47]. Consequently, PhCWs are often used in the slow-light regime [48], where $n_g \approx 58$ has been measured [49]. Unfortunately, in-plane backscattering between the counter-propagating modes scales as n_g^2 [50], resulting in prohibitively large losses at high n_g's. As we discuss below, the backscattering loss also depends on how the electric field is distributed within the PhCW unit cell, opening up a route toward realistic slow-light interfaces.
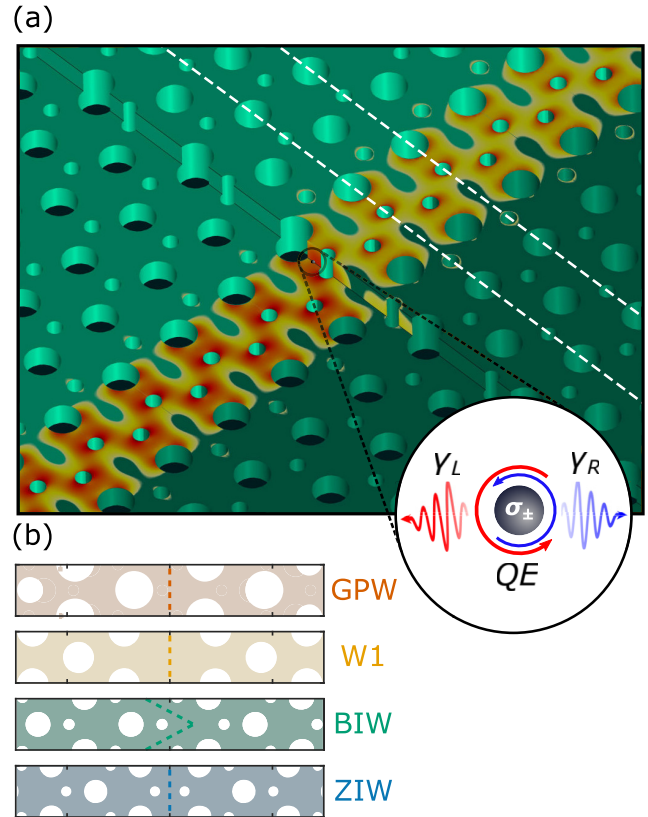

FIG. 1. (a) Schematic of a chiral light-matter interface utilizing an edge mode between two topological photonic insulators (dark and bright green). The field norm for the guided edge-mode is shown (yellow to red) and an embedded quantum emitter indicated. The quantum emitter's transition dipoles are left- or right-handed circular ($\sigma_\pm$), resulting in directional emission (left and right as shown in the inset) when it is placed at a position where the polarization of the guided mode is circular. The white-dashed line highlights a single supercell of the waveguide. (b) Schematics of the supercells of the BIW, ZIW, GPW, and W1 with the interface or center of each waveguide highlighted with a dashed line.

In this work, we study how well four different PhCWs perform in each of the three areas identified above: D, F, and the minimization of backscattering losses. The corresponding unit cell of each structure is shown in Fig. 1(b), with the interface (center) of each waveguide marked. These have been designed and experimentally implemented [24] to guide light near $\lambda = 930$ nm (see Appendix A for further design parameters) for use with high-quality self-assembled Indium Arsenide quantum dots in a Gallium Arsenide membrane [10] with a fixed lattice constant $a = 266$ nm, but their design can readily be scaled [51] for use with any other quantum photonic platform. Similarly, we limit our designs to circular holes but note that in practice more complex and fabricationally challenging shapes such as triangles [52] or shamrocks [8] are possible.

We consider two topological and two conventional PhCW designs. The conventional waveguides are standard photonic crystal line-defect waveguide (W1) [49], and a broken-symmetry GPW that has been optimized to work as a chiral interface [43]. We compare these to topological PhCWs based

on a photonic analog of the quantum valley-Hall effect (QVH) of two photonic topological insulators [24], each characterized by a topological invariant, the valley-Chern number, of opposite sign $C_v = \pm 1/2$ [44]. In analogy with the electronic QVH insulators [53], we expect that the difference between these invariants (here 1) denotes the number of topological interface modes that span the bandgap, although recent experiments suggest the existence of spectral regions where the mode does not afford protection to sharp bends [24]. Regardless, we use QVH insulators as their guided modes are known to lie below the light lines and hence do not couple to the free-space continuum, in contrast to topological PhCWs based on the photonic analog of the quantum spin-Hall effect, whose modes lie above the light line and are therefore leaky [52,54]. Here, we consider QVH waveguide designs formed by bearded-type interface (BIW) and zigzag-type (ZIW) interfaces [55] as shown in Fig. 1(b).

III. PHOTONIC BAND DIAGRAMS AND DISPERSION

We begin by calculating the (photonic) band diagrams and corresponding electromagnetic field distributions for all four PhCWs, using commercially available finite element software (COMSOL Multiphysics; details of the numerical simulations can be found in Appendix B).

We show the guided TE-like bands for the topological and conventional PhCWs in Figs. 2(a) and 2(b), respectively. In each case, the bulk continuum modes are given by the solid regions, while the guided modes are given by solid curves. Additional modes that are close to the continuum and would therefore be leaky, or the higher-order mode of the W1 and GPW are shown by the dashed curves. We also show an exemplary Bloch normalized mode-profile of the electric field $\|\mathbf{e}_{n,k}\|$ for each well-coupled mode of index n, taken for a group index $n_g(\omega_{n,k}) = c/(d\omega_{n,k}/dk) \approx 15$ [cf. circles in Fig. 2(c)], where c is the speed of light, $\omega_{n,k} = 2\pi\nu_{n,k}$ is the eigenfrequency, and k is the wave number.

Several interesting similarities emerge between the dispersion relations of the topologically conventional and topological waveguide. First, both the W1 and ZIW waveguides support one well-coupled mode and others that are poor choices for a quantum interface. The W1 dispersion contains an odd mode [dashed yellow curve in Fig. 2(a)] and the ZIW dispersion contains two modes in close proximity to the bulk modes [dashed blue curves in Fig. 2(b)] that in practice are expected to leak into the continuum. Furthermore, these two modes have a very large mode volume as discussed in the Appendix B, rendering them unsuitable for efficient light-matter coupling. The W1's fundamental mode is highly confined throughout the entire k-space, while the mode-volume of the ZIW mode has a more complex frequency dependence. As discussed in Appendix B, the ZIW mode-width can be either large or small in regions of high n_g.

Likewise, there exist several similarities between the guided modes of the GPW and those of the BIW, as expected since both share the same broken transverse symmetry. The BIW topological edge-mode is comprised of two separate bands, each of which covers a large frequency interval, in much the same way as the guided modes of the GPW [43]. However, the two bands differ in their backscattering losses
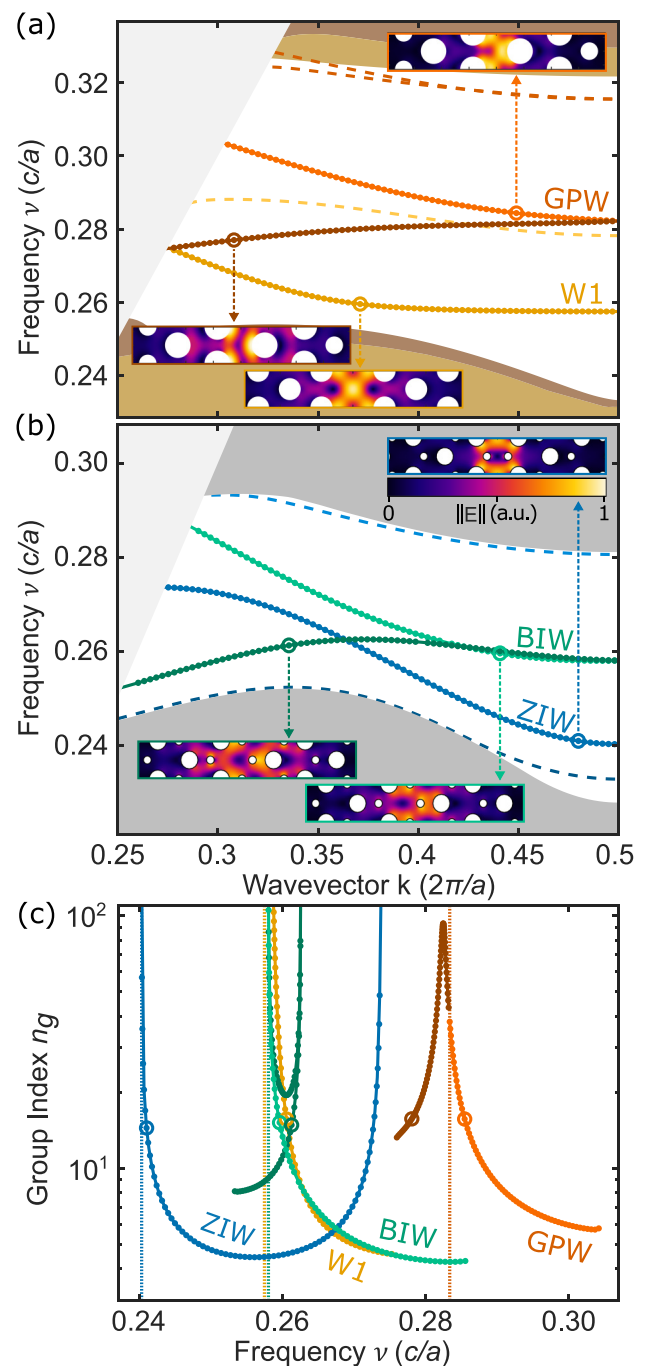

FIG. 2. (a) Photonic band diagram of the GPW (orange) and W1 (yellow) waveguides. Shaded regions correspond to the bulk modes of the GPW (brown) and W1 (yellow), while the gray region represents the light cone. The solid and dashed curves represent guided modes that are considered or excluded in this work, as discussed in the main text. Insets show exemplary mode profiles at $n_g \approx 15$. (b) Same as panel (a) but for topological BIW (green) and ZIW (blue) waveguides, noting that both topological waveguides share the same bulk modes. (c) Group index of the guided modes denoted by solid curves in panels (a) and (b) as a function of frequency for all four structures, with circles representing the modes whose profiles are shown above. The band-edges are indicated by a dotted line.
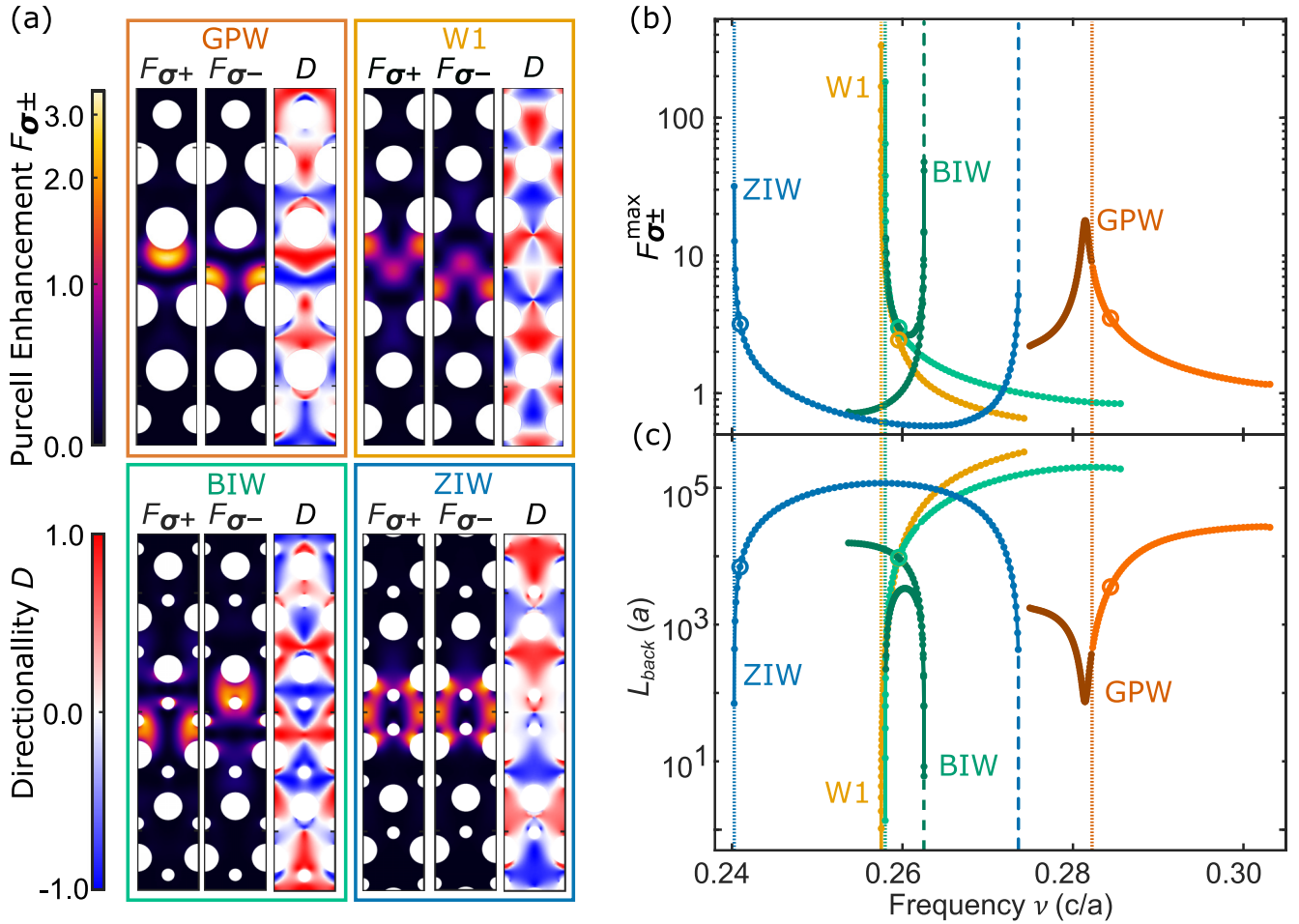
FIG. 3. (a) Mode maps of the directional Purcell factor $F_{\sigma_\pm,k}(\mathbf{r})$ and directionality $D_k(\mathbf{r})$ for a unit cell of each PhCW, taken at $n_g \approx 15$ as shown in Fig. 2(c). (b) Maximal $F_{\sigma_\pm,k}^{\max}$ for each mode as a function of frequency, with dashed curves representing the divergence predicted in the slow-light regions. (c) Corresponding backscattering length $L_{\text{back},n,k}$ in units of the lattice constant a as a function of frequency. Note that both the backscattering losses and interaction enhancement diverge as the group index diverges. The band-edges are indicated by dotted lines, where the group index of all PhCWs except for the GPW diverge. Dashed lines indicate group-index divergences of the band-edge. Circles in panels (b) and (c) represent the modes whose profiles are shown in panel (a).

around bends as demonstrated in measurements and supported by finite-difference time-domain calculations [24]. For 60 degree bends, the upper mode shows little transmission, while near-unity transmission was observed over a large bandwidth of the lower band, making it suitable for the creation of triangular resonators. The two BIW bands cross at $ka/2\pi \approx 0.42$ and are degenerate at the band edge. Both GPW and BIW modes are tightly confined across the entire k-space, with the mode-width of the BIW being significantly larger than that of the GPW and smaller than that of the ZIW, cf. Appendix B. Nevertheless, we find highly confined, slow-light at the band edge of the lower branch of the BIW, indicating that large Purcell enhancement is possible with this structure.

IV. DIRECTIONALITY, PURCELL ENHANCEMENT, AND DISORDER-INDUCED SCATTERING

Having determined the guided modes of each structure, we are now ready to quantify how well each functions as a bright, highly directional and low-loss interface. We begin

by calculating the directional Purcell enhancement $F_{\sigma_\pm,n,k}$ for a left- (subscript $-$) or right-handed (subscript $+$) circular pointlike dipole $\sigma_\pm = 1/\sqrt{2}(\hat{\mathbf{x}} \pm i\hat{\mathbf{y}})$ for each PChW according to Ref. [7]:

$$F_{\sigma_\pm,n,k}(\mathbf{r}) = \frac{3\pi c^2 a n_g(\omega_{n,k})}{2\omega_{n,k}^2 \sqrt{\epsilon(\mathbf{r})}} |\sigma_\pm^* \cdot \mathbf{e}_{n,k}(\mathbf{r})|^2. \quad (2)$$

Although this quantity and others are mode dependent, since in what follows we only consider single-mode operation, the subscript n is omitted for clarity. Exemplary maps of a unit cell of each structure are shown in Fig. 3(a), taken again for modes with $n_{g,n} \approx 15$. From these, we observe that for both the GPW and BIW there is little overlap between $F_{\sigma_+,k}$ and $F_{\sigma_-,k}$. In contrast, these maps differ only near the holes for the W1 structure, and are nearly identical for the ZIW, foreshadowing that these two structures fare poorly as chiral interfaces.

As noted above, the chirality of the interaction is quantified by the directionality,

$$D_k(\mathbf{r}) = \frac{F_{\sigma_-,k}(\mathbf{r}) - F_{\sigma_+,k}(\mathbf{r})}{F_{\sigma_+,k}(\mathbf{r}) + F_{\sigma_-,k}(\mathbf{r})}, \quad (3)$$

examples of which we also present in Fig. 3(a). Here, we observe that while highly directional interactions are possible with all four structures, there is only a high degree of overlap between regions of high Purcell enhancement and directional interactions for the GPW and BIW. For the W1 and ZIW, in contrast, relatively high Purcell factors are found in regions of linear electric field polarization, largely precluding efficient chiral light-matter interactions and showing the importance of breaking inversion symmetry in the waveguides.

We find the maximal Purcell enhancement factor $F_{\sigma_\pm,k}^{\max} = \max_{\mathbf{r} \in \mathbf{S_c}} \{F_{\sigma_\pm,k}(\mathbf{r})\}$ within each map (where S_c denotes the area corresponding to the regions of high-index material), and plot these values as a function of frequency in Fig. 3(b) for all structures. We observe that all structures predict Purcell factors of upwards of 15 away from the band-edge, where both n_g and $F_{\sigma_\pm,k}$ may diverge. In practice, the range of accessible factors is limited by several effects, among them scattering due to structural imperfections [56] and disordered-induced mode broadening [57]). Experimentally, a Purcell enhancement factor of $F \approx 6.9$ has been observed [49], and PhCW systems with significantly higher enhancements have been proposed [58]. From this perspective, all four structures can theoretically enhance a chiral light-matter interaction sufficiently to form the basis of an efficient interface.

A good chiral interface must not only enhance interactions, but must also allow for subsequent low-loss transport. We therefore calculate the ensemble averaged mean-free path (or backscatter loss length) $L_{\text{back},k} = \langle \alpha_{\text{back},k} \rangle^{-1}$, limiting ourselves to the single-mode and single-event backscattering regime as is typical for relatively short waveguides [59]. Here, $\langle \alpha_{\text{back},k} \rangle$ is the power-loss factor per unit cell which is the ensemble average over disorder-induced imperfections (see Appendix C for details and discussion of the scattering mechanisms) for nonuniform air-hole size R_α, where α is the index of the individual holes [60].

We neglect multimode scattering from degenerate modes of the BIW, since their degeneracy can be lifted without significantly altering their mode profile, as was done with the GPW [43], resulting in

$$
\begin{aligned}
\langle \alpha_{\text{back},k} \rangle = \sum_\alpha & \frac{a^2 \omega_k^2 n_g^2 \sigma^2}{4} (\epsilon_2 - \epsilon_1)^2 \\
& \times \iint d\mathbf{r} d\mathbf{r}' \Theta\left(\frac{h}{2} - |z|\right) \Theta\left(\frac{h}{2} - |z'|\right) \\
& \times \delta(R_\alpha - |\boldsymbol{\rho} - \boldsymbol{\rho}_\alpha|)[\mathbf{e}_k^*(\mathbf{r}) \cdot \mathbf{p}_k^*(\mathbf{r})][\mathbf{e}_k(\mathbf{r}') \cdot \mathbf{p}_k(\mathbf{r}')] \\
& \times \exp\left(\frac{-R_\alpha|\tilde{\phi} - \tilde{\phi}'|}{l_p} + i2k(x - x')\right),
\end{aligned} \tag{4}
$$

where σ is the statistical surface roughness factor, Θ denotes the Heaviside function, h is the membrane height, z is the vertical Cartesian coordinate, δ is the Kronecker δ function, ρ (ρ_α) denotes the in-plane projection of the position vector (the individual hole center axis); also, $\mathbf{p}_k$ is the polarizability, l_p is the surface roughness correlation length, and $\tilde{\phi}$ is the azimuth angle of the position vector in the cylindrical coordinate system which is centered in the hole α. In principle, multimode back-scattering can be explicitly included [56]. Yet

TABLE I. Purcell factors $F_{\sigma_\pm}^{\max}$ and mean-free paths L_{back} for the highlighted modes with a group index of $n_g = 15$.

PhCW	$F_{\sigma_\pm}^{\max}$	L_{back}
W1	2.4	$9.4 \times 10^3 \, a$
GPW	3.5	$3.6 \times 10^3 \, a$
ZIW	3.2	$7.0 \times 10^3 \, a$
BIW	3.0	$9.6 \times 10^3 \, a$

is not expected to significantly contribute to losses other then for slow, small k (leaky) modes [56,61].

Considering state-of-the-art soft mask nanofabrication methods [59,62] we assume a surface roughness for each hole of $\sigma = 3$ nm and a correlation length for this disorder within each hole of $l_p = 40$ nm [cf. Fig. 8(b)] and present the resulting mean-free path $L_{\text{back},k} = \langle \alpha_{\text{back},k}^{-1} \rangle$ for all structures in Fig. 3(c). Interestingly, and as we show in Appendix C, the relative performance of the different structures, with respect to backscattering losses is relatively insensitive to the absolute value of l_p. As expected, scattering losses increase with the group index, yet the absolute scattering length can significantly differ for the different structures (and in general does not scale quadratically with n_g [59], as we also show in Appendix D). As an example, for $n_g = 15$, we find the Purcell factors and mean-free paths as listed in Table I.

That is, for this moderate group index all PhCWs show Purcell factors and mean-free paths varying by more than a factor of 2. The W1 and BIW PhCWs show the least losses, while the GPW provides the strongest enhancement factor. As can be seen in the mode distributions [cf. Fig. 2(a)], the field of the W1 PhCW is mainly located in the line defect center, away from the holes (see Appendix D), yet is only weakly circularly polarized [Fig. 3(a)]. The GPW mode is more strongly localized near the hole edges, leading to higher scattering losses, yet it is also circularly polarized at these areas of high field intensity. In contrast, while the field distribution of the BIW is also highest at points of circular polarization, these are located more separated from the holes, reducing backscattering due to imperfections. While the BIW's performance according to Table I may seem similar to the W1, the mode profile shown in Fig. 3 is very alike the GPW's. The relatively lower Purcell factors and the lower losses stem from a wider Bloch mode with relatively lower field strength at the hole interfaces (See Appendix B). Analogously, the ZIW's mode profile is similar to the W1's, but the wider Bloch mode with significant field strength at the hole interface results in a performance reduction.

V. OVERALL PERFORMANCE OF THE CHIRAL INTERFACES

A real quantum chiral light-matter interface must not only simultaneously enhance the interactions with circular transition dipoles and limit subsequent transport losses, but also be designed such that high-quality quantum emitters can be readily embedded in regions where coupling is effective. This places two constraints: (i) the emitters cannot be located too close to the air-dielectric interfaces of the holes so as to avoid
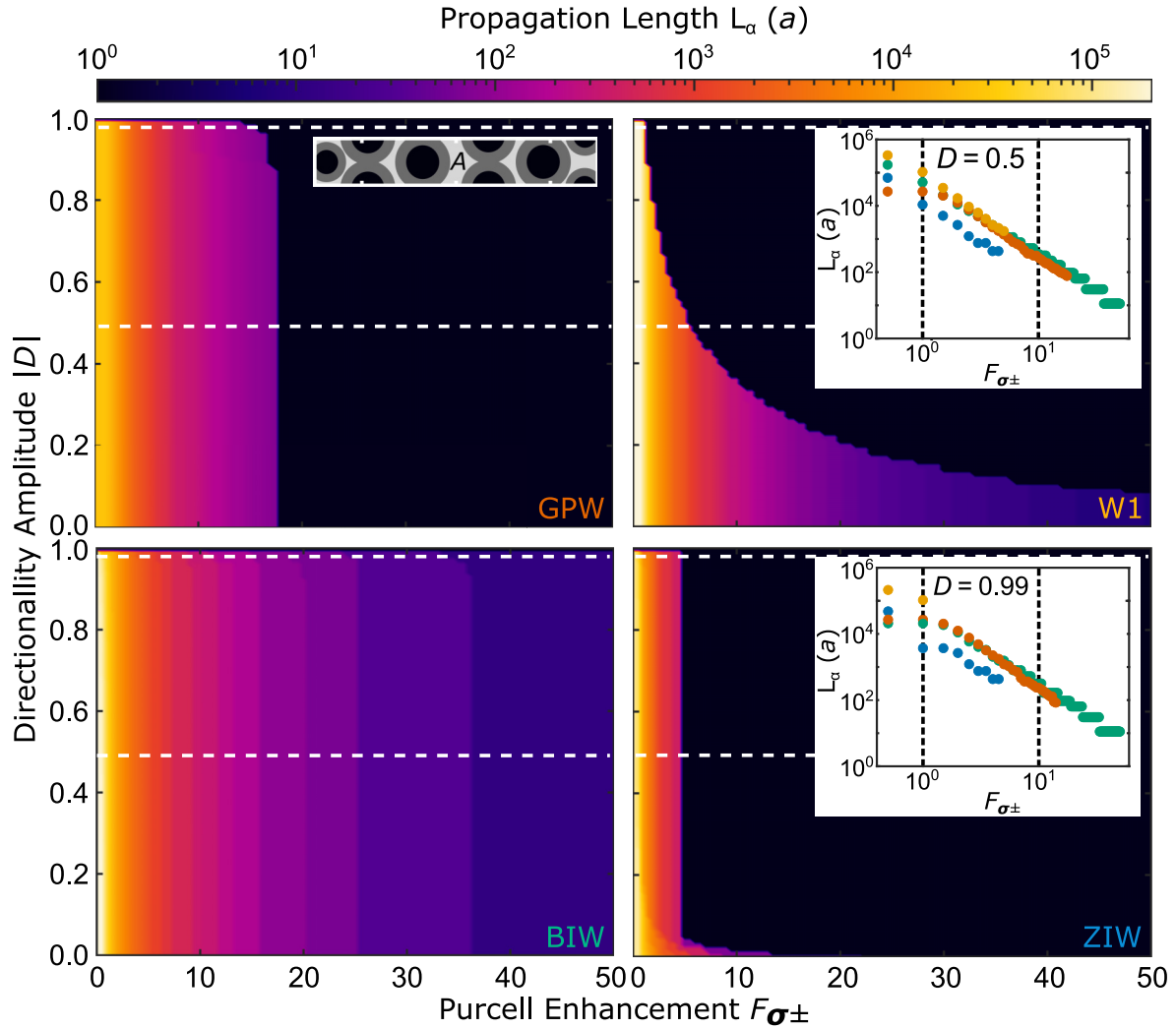
FIG. 4. A summary of PhCW paramaters for use as practical quantum chiral-light matter interfaces. Maps of the maximal achievable propagation length (in units of the lattice constant a) as a function of the minimum desired directionality or Purcell Enhancement factor (structure marked in each panel). This combination of D and F must be found in an area $A \geqslant A_{\min}$, which is sufficiently distant $\delta_{\min}$ from a hole, as sketched in the inset of the first panel and explained in the main text. The bright gray area indicates the area A as an example for the W1, while the dark and black areas indicate the excluded regions given by $\delta_{\min}$. Insets in the W1 and ZIW panels show line cuts showing the propagation length as a function of F for $|D| = 0.5$ and $|D| = 0.99$, respectively (cuts taken along the white dashed lines).

interactions with surface states, and (ii) the area of the region where the emitters can be located should be large enough to ensure a high yield of successful couplings (for details on the spatial constraints see Appendix E). Condition (i) can typically be met with a distance $\delta_{\min} = 40$ nm [63–65], while state-of-the-art nanofabrication protocols allow for the deterministic solid-state emitter-photonic structure integration with an accuracy of around $\delta_{\mathrm{acc}} \approx 40$ nm [66–68].

In Fig. 4 we therefore show the maximal propagation length $L_{\mathrm{back}}^{\max}(F_{\sigma_\pm}, |D|)$ that is possible, for a minimum desired directionality amplitude $|D|$ [69] and Purcell enhancement $F_{\sigma_\pm}$ for each structure with free choice of the mode and wave number k [70], but with the condition that a quantum emitter fits within an area $A_k(F_{\sigma_\pm}, |D|, \delta_{\min})$ of minimum size $A_{\min} = \pi \delta_{\mathrm{acc}}^2$ while all points within this area are at least $\delta_{\min}$ away from the edge of an air hole (for details on the numerical implementation see Appendix E). From this figure it is evident

that only the GPW and BIW will realistically make good chiral light-matter interfaces, as there essentially does not exist a sufficiently large enough area to couple an emitter to either a W1 or ZIW structure with high directionality and even a moderate $F_{\sigma_\pm} = 5$ ($F_{\sigma_\pm} = 3$) for the ZIW (W1) (although, for a ZIW, these points do exist within $\delta_{\min}$ of the air holes). In contrast, sufficiently large areas can be found within unit cells of the GPW and BIW where both near-perfect directionality ($|D| \geqslant 0.99$) and enhancements up to $F = 14$ and beyond are possible.

Where the topological BIW distinguishes itself from the GPW is both in the size of the area that can be used to efficiently and chirally interface to emitters, and in its performance at enhancement factors exceeding 14. For fixed $|D| = 0.99$ and $F_{\sigma_\pm} \leqslant 10$ areas of at least 7.6×10^5 nm^2 (corresponding to a circle of radius $R_{|D|=0.99} \approx 491$ nm) can be found within a GPW unit cell, while for this area a BIW is

limited to 4.4×10^4 nm^2 (corresponding to a circle of radius $R_{|D|=0.99} \approx 118$ nm). This can be seen in Appendix E, where we also discuss how this area is determined.

Figure 4 shows that for high directionality $|D| = 0.99$ the GPW outperforms the BIW as a chiral interface by about 30 % higher propagation lengths, if low interaction enhancements $F_{\sigma_\pm} \leqslant 4$ are desired. For intermediate Purcell enhancements $(4 \leqslant F_{\sigma_\pm} \leqslant 12)$ the GPW and the BIW show similar losses, while for higher interaction enhancements $(F_{\sigma_\pm} > 12)$ the propagation length of the BIW is longer than that of the GPW. The highest achievable Purcell enhancement for the GPW is $F_{\sigma_\pm} = 17.5$ (14) for a minimal directionality amplitude $|D| = 0.5$ $(|D| = 0.99)$. It is important to recognize that this limit arises due to the dispersion engineering of the GPW, which causes its group index to remain finite in the entire reciprocal space, in contrast to an unoptimized GPW whose dispersion relation diverges at the lower band edge [43].

The difference between the losses of the GPW and BIW can be understood by considering their respective mode profiles (cf. Appendix B), and realizing that in general the light is better confined in the GPW compared to the BIW. Particularly for low to intermediate group indices we find that the mode width of the GPW is half, or less, than that of the BIW (cf. Appendix B). In the GPW, we can thus find the same enhancement as in the BIW for lower n_g's, and hence less scattering losses. However, for large group indices the Bloch mode profile of the GPW's shows high intensity near the first air-hole row leading to a strong relative increase of the backscattering losses (cf. Appendix D). In other words, for low Purcell enhancements the GPW's disadvantage of high backscattering losses are compensated by tighter mode confinement. For example, for $|D| = 0.99$ we find a propagation length of $20880a$ $(51330a)$ for a Purcell enhancement of $F = 1$, and $318a$ $(240a)$ for a Purcell enhancement of $F = 10$ for the BIW (GPW). This means less than 4 % (5 %) backscattering losses for a 10-unit cell long waveguide and out-of-plane scattering dominating for low Purcell enhancements [71].

VI. CONCLUSIONS

From the selected photonic crystal waveguides studied, only the GPW and the topological BIW are suitable platforms for chiral quantum optics. Both of these designs can enhance highly directional interactions for emitters located in relatively large regions. Both designs suffer from backscattering due to fabrication impurities, although the topological waveguide offers protection to 60-degree bends [25,32–34], enabling sharp-edge microresonators that do not suffer from bending losses [19,24,72–74].

The ability of these structures to act as elements in viable quantum chiral light-matter interfaces is perhaps easier to visualize using a concrete example. Here, we consider the performance of a single quantum emitter chirally interfaced with a PhCW. This fundamental element enables realization of integrated nonreciprocal single-photon devices for constructing of scalable complex quantum circuits and networks [10]. Examples are loss-tolerant two-qubit measurements [16], optical

isolators and circulators [8,11], photon number dependent routing [75–77], $\sqrt{\text{SWAP}}$ [9] and CNOT gates [78].

Specifically, we assess the setting where single photons are injected into the PhCW in which the chirally coupled quantum emitter coherently (and asymmetrically) scatters the injected photon forward or backward [45]. The forward propagating photons are single-sidedly collected after transmission through the PhCW of N_α unit cells.

The speed with which such a element ideally operates is set by the characteristic rate of the emitters, namely, their decay rates: $\gamma_{R/L} = \gamma_{R/L}^0 F_{\sigma,\pm}$, where $\gamma_{R/L}^0$ is the quantum emitter's directional emission rate in a homogeneous medium. In reality, the circuit operation rate (and fidelity) will be further decreased as photons are lost to scattering due to imperfections or imperfect directionality. Assuming backscattering only, the intensity, or accessible photon flux $\Phi_{R/L}$, is thus given by

$$\Phi_{R/L} = \gamma_{R/L}^0 F_{\sigma_\pm} \exp\left[-\frac{N_a}{L_{\text{back}}^{\max}(F_{\sigma_\pm}, |D|)} \right], \qquad (5)$$

where we explicitly note that the maximum propagation length (in units of a) is a function of the desired enhancement and directionality.

We set $|D| = 0.99$ as for near ideal chiral coupling. We consider two limiting cases, a 10-unit cell PhCW ($\approx 2.7\,\mu$m for our structures) which is the shortest length to act as a proper interface [58] and a 100 unit cell waveguide ($\approx 27\,\mu$m) which is a more typical length in current circuits [8], and plot $\Phi_{R/L}/\gamma_{R/L}^0$ as a function of $F_{\sigma_\pm}$ in Figs. 5(a) and 5(b), respectively. The performance of the shorter structures is limited by the maximum achievable Purcell Factor (cf. Fig. 4), and we observe losses of less than 1% for both GPW and BIW for $F \leqslant 2$ which increase to 10% at around $F = 13$. For higher values of F operation is only possible with the BIW, and we expect 15% losses at $F = 20$. That is, for the shorter interfaces, low loss operation is compatible with moderate interaction enhancement. Here, we note that $\Phi_{R/L}$ can directly quantify device performance, with the exact dependence determined by how many chiral elements are needed and the specific protocol (e.g., whether it depends on emission or transmission). For example, the operation speeds of quantum networks for all optical routing of single photons [14] and loss-tolerant two-qubit measurements capable of universal quantum computation [16] is determined by the accessible photon flux directly, $\Phi_{R/L}$, showing that GHz rate operation is possible.

For the longer devices we calculate about 1% losses for the BIW and GPW, respectively, at $F = 2$, which increase to 27% and 34% at $F = 10$. At $F = 20$, where only the BIW can be used, we expect upwards of 79% losses, resulting in characteristic photon rates of $\Phi_{R/L}/\gamma_{R/L}^0 \approx 4$. Thus while even the longer waveguides can serve as chiral elements in quantum photonic circuits, for most efficient operation one should opt for a short, topologically protected waveguide.

Finally, we note that the topological waveguides considered here have not been optimized, in contrast with the GPW [43]. Several methods can be used to optimize their directionality and losses [59,79–82]. All rely on dispersion engineering, where changing the size, shape, or position of
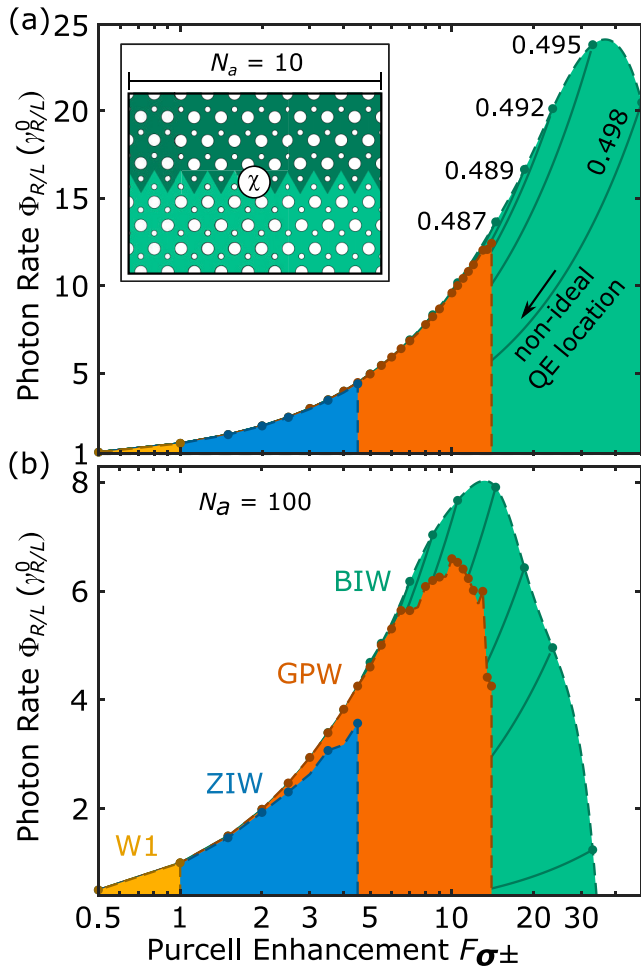
FIG. 5. Calculated delectable photon flux, in units of the homogeneous decay rate, as a function of the Purcell enhancement for a quantum emitter χ chirally coupled to a PhCW as shown in the inset to panel (a) [16]. The photon rate is shown for (a) short, 10-unit cell structures and (b) the more typical 100-unit cell waveguides in solid circles resolution limited by the *k*-space sampling, which are labeled as an example for the BIW for the data points of highest Purcell enhancements, cf. Appendix F). The dashed lines represent a guide to the eye, while the solid curves represent a sub-optimal positioning of the QE. In both panels (a) and (b), the performance of all 4 structures is shown, with the topological BIW supporting highest-rate operation. This is true both for the shorter systems, where losses are low in all cases, as well as for the longer structures, where the high n_g (enhancement) operation is limited by the scattering.

the holes modifies both the band-structure and field distributions, enabling slow light single-mode operation away from the bulk modes or pushing the electric field distribution away from the holes [25,28,52,79,83,84]. Doing so will reduce both backscattering and out-of-plane scattering while allowing for efficient and directional interactions.

ACKNOWLEDGMENTS

APPENDIX A: PHOTONIC CRYSTAL PARAMETERS

All PhCWs's parameters can be rescaled with the crystal lattice constant *a*. For numerical implementation we have set $a = 266$ nm and a membrane thickness of $h = 170$ nm. We have set the refractive index of the high-index membrane to $n_1 = 3.4638$ and in the surrounded by vacuum $n_2 = 1$, representing a GaAs-based platform in cryogenic conditions ($T = 4$ K) [85].

A schematic of all PhCWs's parameters shown in Fig. 6. For the W1 have set a hole radius of $r/a = 0.3$. For the GPW, we follow the proposed design parameters [43]. The center hole-to-hole distance is $d = 0.75\sqrt{3}\,a$. The radii r_i and outwards position shifts l_i of the first four rows of index i of air holes are $r_1/a = r_2/a = 0.35$, $r_3/a = 0.24$, $r_4/a = 0.3$, and $l_1/a = 0$, $l_2/a = \sqrt{3}/8$, $l_3/a = \sqrt{3}/10$, $l_4/a = \sqrt{3}/20$. The other rows are not shifted in position and have a hole radius identical to the fourth hole row radius r_4. The latter is identical to a W1's hole radii of $r/a = 0.3$. The topological photonic insulator's unit cell (BIW and ZIW) consists of two holes of radius of $r_1/a = 0.105$ and $r_2/a = 0.235$, resembling an experimental implementation of a chiral light-matter interface [24].
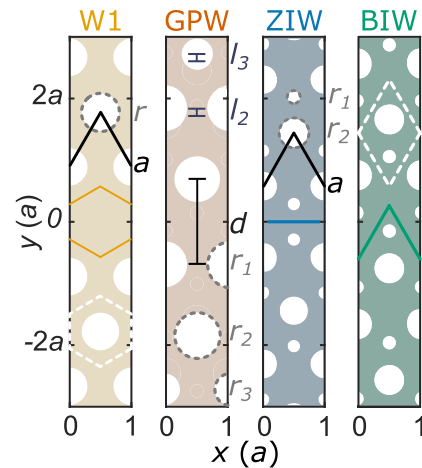

FIG. 6. Schematic of the waveguide center region of the PhCWs's supercells and their parameters for the simulations, as discussed in the text. Each photonic crystal border lines are highlighted in color. Hole radii are indicate in gray. The GPW's photonic crystal is deformed from the W1 in the PhCW's center region as discussed in the text. The deformation parameters are indicated and labeled in gray. The deformation parameters r_4 and l_4 of the GPW is outside the shown region. The lattice vectors (photonic crystal's unit cells) are indicated for the W1 and the topological waveguides in a solid black (white dashed) line. The ZIW's and BIW's photonic crystals have the same unit cell and lattice vectors but their interface follows along different directions.

APPENDIX B: FEM CALCULATIONS SETTINGS, BLOCH MODE NORMALIZATION, GROUP INDEX, AND MODE WIDTH CALCULATIONS

We performed numerical finite element calculations (FEMs) to determine the PhCW's Bloch modes and eigenvalues. The PhCWs are systems of mixed dielectric media for which we can compute the steady state solutions of the Maxwell equations resembling linear Hermitian eigenvalue problems [51] by using the commercial software COMSOL Multiphysics.

For each type of PhCW, a supercell of the one-dimensional periodic structure was studied using periodic boundary conditions (PBC). With a perfect magnetic conductor (PMC) plane, aligned with the reflection symmetry plane of the waveguides the numerical complexity is simplified limiting the study to transverse electric (TE) modes only. This takes the in-plane electric dipole moments of QEs suitable for chiral light-matter interaction [10] and TE-like mode profiles of the discussed PhCWs into account [28,43,51]. The simulated volume was restrained by perfectly matched layers (PML) below the membrane and each side of the PhCWs. The distance between the waveguide center and the PML below the membrane and on the sides of the PhCWs was chosen to achieve negligible mode leakage into the PML with a width of $12\sqrt{3}a$ on each side. Numerical convergence was tested sweeping the maximal element size of the mesh grid the Master's equation was solved for. This resulted in a tetrahedral mesh with a locally maximal element edge length of $1/10$ of the minimal distance between any local interface of differing dielectric constants.

We defined a right-handed Cartesian coordinate system with $\hat{x}$ being aligned with direction of propagation in the waveguide, $\hat{y}$ pointing into the plane of the 2D photonic crystal and $\hat{z}$ pointing out of plane, i.e., normal to the membrane.

We sampled the k-space of the PhCW in increments of $\Delta k = 0.003 \cdot 2\pi/a$ and computed the electric $\mathbf{e}_{n,k}(\mathbf{r})$ Bloch modes [with magnetic field $\mathbf{h}_{n,k}(\mathbf{r})$] and eigenfrequencies $\nu_{n,k} = \omega_{n,k}(k)/2\pi$ of each Bloch mode n of wave number k. For clarity we omit the mode index in the following. We also omit solutions in the light cone. We satisfy the Bloch mode normalization:

$$\int_{\mathcal{V}_s} d\mathbf{r} \, \|\mathbf{e}_k(\mathbf{r})\|^2 \epsilon(\mathbf{r}) = 1, \tag{B1}$$

where $\|\mathbf{e}_k(\mathbf{r})\|$ is the norm of the electric field of the Bloch mode and $\epsilon = n^2$ is the dielectric constant. We determine the group index for each mode $n_g(\omega_k) = c\frac{d}{dk}\omega_k$ using the Hellmann-Feynmann theorem [86]:

$$n_g(\omega_k) = \frac{2c(U_{\mathbf{e},k} + U_{\mathbf{h},k})}{|\int_{\mathcal{V}_s} d\mathbf{r} \, \text{Re}[\mathbf{e}_k^*(\mathbf{r}) \times \mathbf{h}_k(\mathbf{r})]|}, \tag{B2}$$

where c is the speed of light, $\mathcal{V}_s$ is the total super-cell volume, and $U_{\mathbf{e},k}$ ($U_{\mathbf{h},k}$) is the time averaged electric (magnetic) field energy.

We define and evaluate a characteristic mode width measure w_k (shown in Fig. 7) as the volume integral of the electric energy density $u_{\mathbf{e},k}(\mathbf{r})$ [magnetic $u_{\mathbf{h},n,k}(\mathbf{r})$ density]. We assigned the mode width measure w_k implicit by the volume $\mathcal{V}_w = \{\mathbf{r} \in \mathcal{V}_s : -w_k < \mathbf{r} \times \hat{y} < w_k\}$ such that the time-averaged field energy inside the integration volume $\mathcal{V}_w$ is $1/e$ of the time-averaged field in the entire supercell
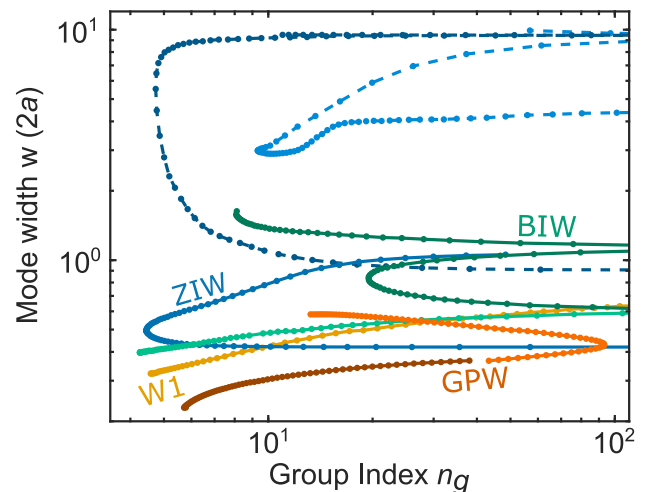

FIG. 7. Characteristic mode width w_n as a function of the group index $n_g(\omega_{n,k})$ of all band-gap modes of the BIW, ZIW and the selected modes of the GPW and W1 for comparison. The data points are connected along their individual wave number k. The dashed lines correspond to the modes of the ZIW which are not considered for a chiral-light interface due to their extreme mode widths.

volume $\mathcal{V}_s$:

$$\int_{\mathcal{V}_w} d\mathbf{r} \, \frac{u_{\mathbf{e},k}(\mathbf{r}) + u_{\mathbf{h},k}(\mathbf{r})}{U_{\mathbf{e},k} + U_{\mathbf{h},k}} = \frac{1}{e}, \tag{B3}$$

where $u_{\mathbf{e},k}(\mathbf{r})$, $u_{\mathbf{h},k}(\mathbf{r})$ are the electric and magnetic field energy density and $\mathcal{V}_w = \{\mathbf{r} \in \mathcal{V}_s : -w_k < \mathbf{r} \times \hat{y} < w_k\}$ is the effective mode volume.

The tight confinement of the GPW stems from the modified hole radii and position, and the modification of the space between the photonic crystals. The BIW's and ZIW's modes vary drastically in their characteristic mode width compared to topological trivial PhCWs and deviate clearly from the trend of increasing mode volume with increasing group index as observed for the W1. The GPW's lower frequency modes deviates from this trend only slightly.

APPENDIX C: INCOHERENT BACKSCATTERING POWER-LOSS FACTOR CAUSED BY STRUCTURAL DISORDER

Beyond intrinsic losses of the dielectric medium, guided modes of PhCW experience further losses, which arise from photon-scattering. In the most general case, a guided mode of a PhCW experiences out-of-plane losses (scaling approximately with n_g) and in-plane scattering losses into bulk modes and reverse propagation modes (scaling approximately with n_g^2) [50,59]. For sufficiently large group indices, the out-of-plane can be neglected [61]. Scattering into bulk modes can be suppressed by lifting the frequency region of interest away from the bulk by choice of the lattice parameters and by photonic band engineering [79,84]. Furthermore, the single-mode operation of a PhCW can also be achieved by photonic band engineering [25,28,52]. Yet, in contrast to systems with broken TRS, backscattering losses in systems obeying TRS

cannot be eliminated due to the guaranteed double degeneracy of the modes in forward (k) and backwards propagation ($-k$) [69]. Consequently, backscattering between these two modes is allowed. While there are indications of a potentially exploitable advantage of topological waveguides to be less sensitive to defects of the same symmetry group as the corresponding Hamiltonian [28,44], we assume backscattering to be caused by isotropic fabrication induced disorder in good agreement with theory and experiment [50]. As discussed in Sec. IV, we assume the single-event backscattering regime as is typical for relatively short waveguides [59].

The ensemble average $\langle \alpha_{\text{back}} \rangle$ of the fabrication disorder-induced single-event incoherent backscattering power loss per unit cell α_{back} can be calculated semi-analytically using the slowly varying surface approximation [50,87]. For a short W1 ($< 100\,\mu\text{m}$) and group index of about $n_g < 22$, α_{back} is the backwards reflections loss described by the Beer-Lambert relation [56]. For higher group indices or longer waveguides, the Beer-Lambert relation overestimates the backwards reflections for long waveguides due to multiple-scattering. In the multiple-scattering regime the effective losses per unit cell decreases to $\alpha_{\text{back}}^{\text{eff}} = \alpha_{\text{rad}}\sqrt{1 + 2\alpha_{\text{back}}/\alpha_{\text{rad}}}$ where α_{rad} is radiative loss [56]. For our discussion, we assume PhCWs of minimal length to form a chiral light-matter interface to achieve minimal losses. Therefore, we omit multiple-scattering events. PhCWs as short as 10-unit cells are sufficient for high quality light-matter interfaces [58]. We neglect the out-of-plane scattering losses, taking the scaling only linear in n_g into account [56].

We also neglect multimode scattering as discussed in the main text and therefore find the backscattering power loss factor per unit cell by adaption from Patterson and Hughes [88] to be

$$\alpha_{\text{back},k} = \frac{a^2 \omega_k^2 n_g^2(\omega_k)}{4} \iint d\mathbf{r} d\mathbf{r}' \Delta\epsilon(\mathbf{r})\Delta\epsilon(\mathbf{r}')$$
$$\times [\mathbf{e}_k^*(\mathbf{r}) \cdot \mathbf{p}_k^*(\mathbf{r})][\mathbf{e}_k(\mathbf{r}') \cdot \mathbf{p}_k(\mathbf{r}')]\exp[i2k(x - x')], \tag{C1}$$

where $\Delta\epsilon(\mathbf{r})$ describes the difference of the dielectric function between the ideal and disordered structure and $\mathbf{p}_{n,k}$ is the polarization density:

$$\mathbf{p}_k(\mathbf{r}) = \left[\mathbf{e}_{k,\parallel}(\mathbf{r}) + \epsilon(\mathbf{r})\frac{\mathbf{d}_{k,\perp}(\mathbf{r})}{\epsilon_1 \epsilon_2} \right] \delta(\mathbf{r} - \mathbf{r}'), \tag{C2}$$

where $\mathbf{e}_{k,\parallel}$ is the electric field components of the Bloch mode parallel to interfaces of changing dielectric constants $\epsilon_1 = n_1^2$ and $\epsilon_2 = n_2^2$ and $\mathbf{d}_{k,\perp}$ is perpendicular electric displacement fields. This disorder form satisfies the correct boundary conditions at the hole interface.

We assume in-plane hole deformation of ΔR of the holes to be the dominant source of scattering in good agreement with theory and experiment [56,71]. Thus $\Delta\epsilon(\mathbf{r})$ is only nonzero at the hole walls. With air hole indices α and the corresponding hole's Radius R_α, we can write the change of the dielectric function as

$$\Delta\epsilon(\mathbf{r}) = (\epsilon_2 - \epsilon_1)\Theta\left(\frac{h}{2} - |z|\right) \sum_\alpha \Delta R[\tilde{\phi}(\boldsymbol{\rho}, \boldsymbol{\rho}_\alpha)]$$
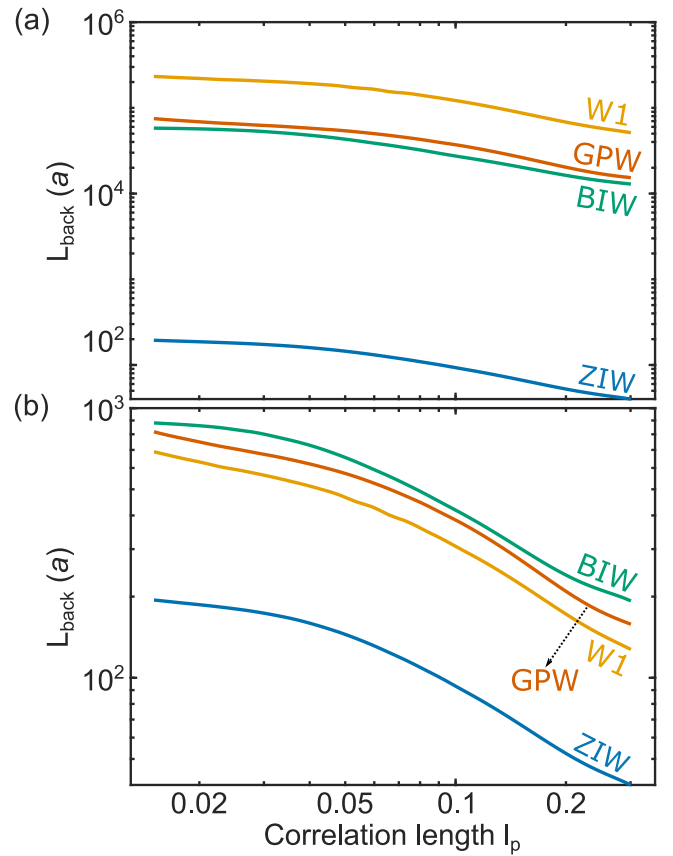$$\times \delta(R_\alpha - |\boldsymbol{\rho} - \boldsymbol{\rho}_\alpha|), \tag{C3}$$

FIG. 8. Inelastic mean-free path $L_{\text{back},k} = \langle \alpha_{\text{back},k} \rangle^{-1}$ sweeping the correlation constant l_p and keeping the deformation parameter $\sigma = 3\,\text{nm}$ constant for chosen modes representing minimal backscattering fullfilling the requirements of: (a) providing Purcell enhancement $F = 1$ and a directionality $|D| = 0.99$ in locations being separated from hole by δ within the high-index regions of the vertical symmetry plane $\mathcal{S}_c$ (see Appendix E) and (b) providing a Purcell enhancement $F = 10$ and providing the highest direcionality D_{max} accessible for each PhCW within the same position restrictions as in panel (a). The inlet shows a schematic of the stastical hole deformation parameters. A hole is deformed by a dent of amplitude σ over a correlation length l_p.

where $\boldsymbol{\rho}$, $\boldsymbol{\rho}_\alpha$ are the in-plane vectors to $\mathbf{r}$ and the hole center position of hole α, and where $\tilde{\phi}$ is the angular coordinate of the position $\mathbf{r}$ in the cylindrical coordinate system centered in the hole α, so that

$$\tilde{\phi}(\boldsymbol{\rho}, \boldsymbol{\rho}_\alpha) = \arctan\left[\frac{\boldsymbol{\rho}\sin(\phi) - \boldsymbol{\rho}_\alpha\sin(\phi_\alpha)}{\boldsymbol{\rho}\cos(\phi) - \boldsymbol{\rho}_\alpha\cos(\phi_\alpha)}\right]. \tag{C4}$$

We assume disorder between different air holes α_i and α_j to be uncorrelated for $i \neq j$ but to be perfectly correlated within each air hole in the cylindrical axis direction. This assumption takes the statistical functions determined by imaging of photonic crystal slabs into account [62]. We can write the disorder correlation between two points of the sidewall as

$$\langle \Delta R(\tilde{\phi})\Delta R(\tilde{\phi}') \rangle = \sigma^2 \exp\left(\frac{-R_\alpha|\tilde{\phi} - \tilde{\phi}'|}{l_p}\right)\delta(\alpha, \alpha'). \tag{C5}$$

Thus, the ensemble averaged incoherent disorder-induced backward scattering power loss per unit cell in the single-scattering event approximation omitting multimode scattering is then

$$
\langle \alpha_{\text{back},k} \rangle = \sum_{\alpha} \frac{a^2 \omega_k^2 n_g^2(\omega_k) \sigma^2}{4} (\epsilon_2 - \epsilon_1)^2
$$
$$
\times \iint d\mathbf{r} d\mathbf{r}' \Theta\left(\frac{h}{2} - |z|\right) \Theta\left(\frac{h}{2} - |z'|\right)
$$
$$
\times \delta(R_\alpha - |\boldsymbol{\rho} - \boldsymbol{\rho}_\alpha|)[\mathbf{e}_k^*(\mathbf{r}) \cdot \mathbf{p}_k^*(\mathbf{r})][\mathbf{e}_k(\mathbf{r}') \cdot \mathbf{p}_k(\mathbf{r}')]
$$
$$
\times \exp\left(\frac{-R_\alpha |\tilde{\phi} - \tilde{\phi}'|}{l_p} + i2k(x - x')\right). \quad \text{(C6)}
$$

This formalism recovers the approximate backscattering scaling quadratic in the group index. However, the backscattering is highly dependent on the PhCW's morphology by means of the intensity profile at the air-hole walls, and the Bloch modes change as a function of frequency and k [59]. Mode profiles with high field strengths at a large number of holes show high backscattering losses. Similarly, small holes are associated with larger backscattering losses due to the R_α/l_p term, as they occur in the third row of holes in the GPW and the throughout the BIW's and the ZIW's photonic crystals.

While all WG scale quadratically in σ the effect of l_p is non trivial, depending on the hole sizes and the field amplitude at the air-hole interfaces. However, the influence of the backscattering parameters seems to be low and affects all PhCWs similarly as shown in Fig. 8 where we show the in-elastic mean-free path $L_{\text{back},k} = \langle \alpha_{\text{back},k} \rangle^{-1}$. Thus, the choice of the correlation length and the deformation strength do not influence the choice of the waveguide topology significantly.

APPENDIX D: BACKSCATTERING AND PURCELL ENHANCEMENT SCALING IN THE GROUP INDEX

Upon renormalization of the Purcell enhancement and of the mean free path by their inverse explicit group index dependence, the significance of the dispersion of the mode profiles and their polarization is revealed as shown in Fig. 9. We observe variations in the mode dependence of the renormalized enhancement (mean-free path) vary up to a factor 4 (20) throughout the full k-space outside the light cone. For identical group index the implicit group index dependence is taken into account. Still, we find variations in the mode profile dependence of the renormalized enhancement (mean-free path) vary up to a factor 4 (9). The mode profile dependence of both properties does not correlate among different PhCW and their relative dependence is highly dispersive.

APPENDIX E: AREAS OF PURCELL ENHANCEMENT AND DIRECTIONALITY

To compare the PhCWs' performances as quantum emitter based chiral light-matter interfaces, we can compare the maximal propagation length $L_{\text{back},n,k}$ under free choice of the mode and free choice of wave number k for which we find a nonzero area in which we find a minimal directionality D
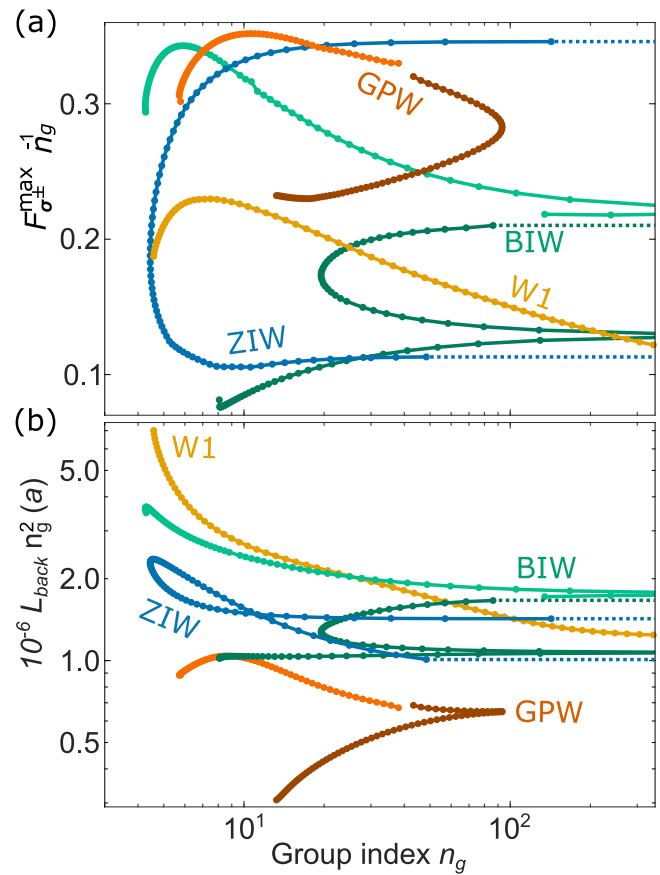

FIG. 9. (a) Renormalized maximal Purcell enhancement $F_{\sigma_\pm,k}^{\max}/n_g$ within the high-index regions of the vertical symmetry plane $\mathcal{S}_c$ (see Appendix E) and (b) renormalized mean-free path $L_{\text{back},k} n_g^2$. The solid lines connect modes along the wave number k while the dashed lines indicate regions of divergence. The nontrivial dispersion of the renormalized Purcell enhancement and the renormalized mean-free path indicate the significance of the dispersion of the mode profiles and their polarization.

and Purcell enhancement F. The free choice of wave vector k and mode n means to tune the PhCW optimally to resonance with the QE by tuning the lattice parameters [70]. However, for a realistic platform, we have to take two more restrictions of QE positioning into account. State-of-the art fabrication techniques only allow for placing QE only at certain minimal distance $\delta_{\min}$ from any air-hole wall interface and only with a certain positioning accuracy δ_{acc}.

Experimentally, the minimum air hole distance has been estimated for near-infrared InGaAs QDs to be about $\delta_{\min} = 30$ nm [68]. We take this restriction of positioning QDs mathematically into account by only considering points in the manifold $\mathcal{S}_{\min}$, defined as all points of the symmetry plane of the high index material $\mathcal{S}_c$ that have a minimal distance $\delta_{\min}$ to any air hole:

$$
\mathcal{S}_{\min}(\delta_{\min}) = \{\mathbf{r} \in \mathcal{S}_c : \|\boldsymbol{\rho} - \boldsymbol{\rho}_\alpha\| \geqslant R_\alpha + \delta_{\min}\}, \quad \text{(E1)}
$$

where $\mathcal{S}_c$ is the high index material region of the PhCWs vertical symmetry plane of the super-cell, and $\boldsymbol{\rho}$ ($\boldsymbol{\rho}_\alpha$) is the in-plane vector to $\mathbf{r}$ (the center of hole with index α).
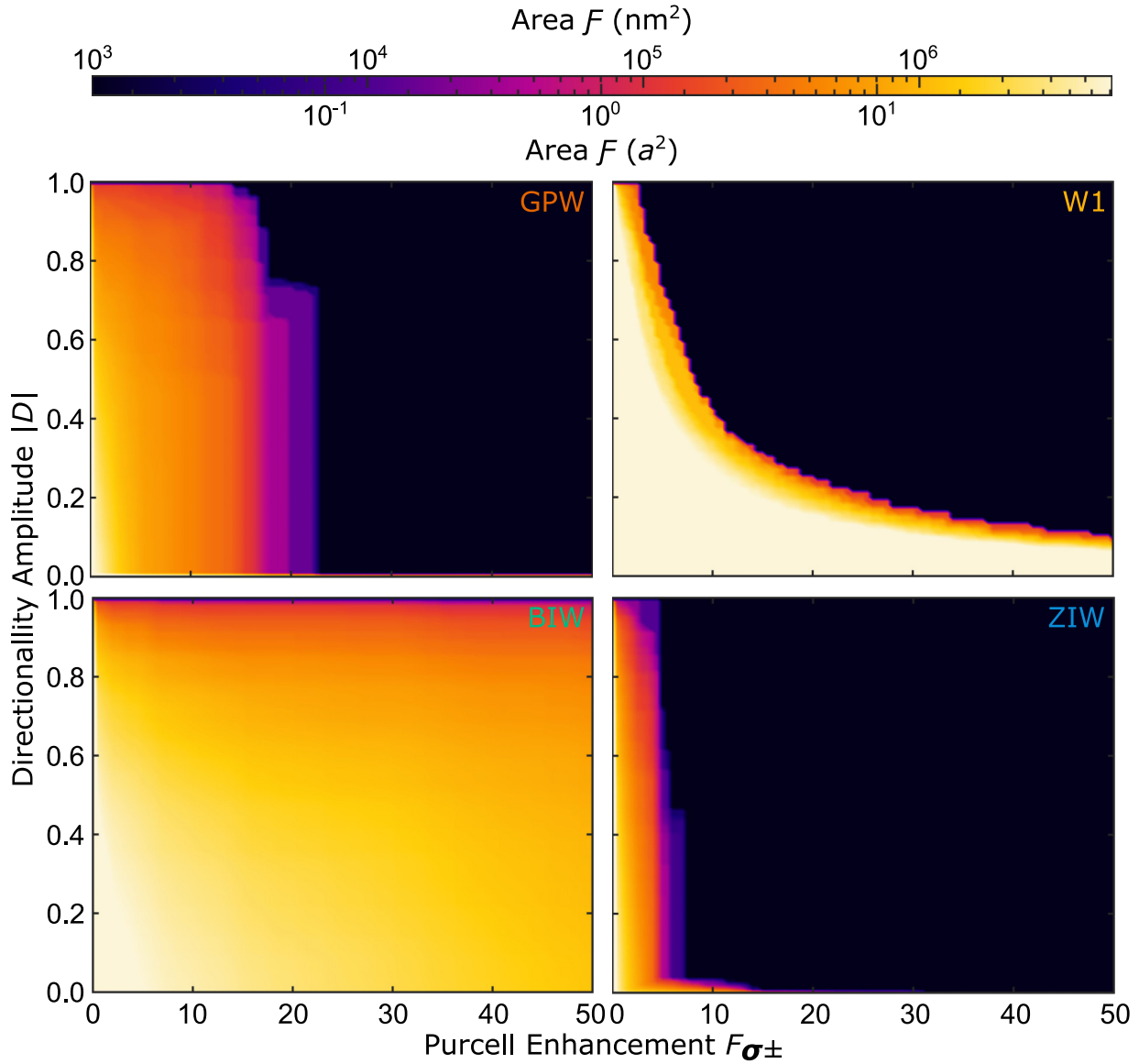
FIG. 10. Maximal area $\mathcal{F}$ of all modes for minimal directionality amplitude $|D|$ and minimal Purcell enhancements P in the high index material area given by $\mathcal{S}_{\min}$, not limiting the associated group index or backscattering losses.

The area $A_k(|D|, F, \delta_{\min})$ of a minimal directionality $D_k(\mathbf{r}) > |D|$ and Purcell enhancement $F_{\sigma_{\pm},k}(\mathbf{r}) > F$ per super-cell considering the QD positioning restriction given by $\delta_{\min}$ is

$$A_k(|D|, F, \delta_{\min}) = \int_{\mathcal{S}(\delta_{\min})} d\mathbf{r} \, \Theta[F_{\sigma_+,k}(\mathbf{r}) - F] \Theta[D_k(\mathbf{r}) - |D|],$$
(E2)

where Θ is the Heaviside step function.

In Fig. 10 we show the maximal areas $A_k(|D|, F, \delta_{\min})$ for a Purcell enhancement F and Directionality D under free choice of the mode and the wave number k:

$$\mathcal{F} = \max_k \{A_k(|D|, F, \delta_{\min})\}.$$
(E3)

We find the W1 to show large areas for high Purcell enhancements but due to its predominately linear polarization throughout the k-space, it does not allow for Purcell enhancements and high directionality for $F > 3$. The ZIW is very similar to the W1 in this regard, although the areas A are for all pairs D, F at least an order of magnitude smaller. The GPW and BIW seem to be similar. However, for areas as of $|D| > 0.9$ ($|D| < 0.9$) the GPW (BIW) offers more area for most pairs D, F. The BIW is the only PhCW allowing for QE interfaces with significant directionality and the highest Purcell enhancement of $F > 20$.

We take the QE positioning accuracy δ_{acc} into account by only considering areas $A_k(|D|, F, \delta_{\min})$ large enough to place a QD within the minimum area $A_{\min}(\delta_{\mathrm{acc}}) = \pi \delta_{\mathrm{acc}}^2$. The

precision of placing a InGaAs QD in a photonic structure is estimated to be about $\delta_{\text{acc}} = 40\,\text{nm}$ [68].

Taking both fabrication limitations into account, we assess the maximal propagation length $L_{\text{back}}^{\max}(F, |D|)$ under free choice of the wave number k and free choice of the mode for which we find an area $A_k(|D|, F, \delta_{\min}) > A_{\min}(\delta_{\text{acc}})$ of a minimal directionality amplitude $D_k(\mathbf{r}) > |D|$ and minimal Purcell enhancement $F_{\sigma_{\pm}, k}(\mathbf{r}) > F$ and take the QE positioning limitations into account as

$$L_{\text{back}}^{\max}(|D|, F, \delta_{\min}, \delta_{\text{acc}})$$
$$= \max_k\{L_{\text{back}, k} : A_k(|D|, F, \delta_{\min}) > A_{\min}(\delta_{\text{acc}})\}. \quad \text{(E4)}$$

We show the conditional maximal propagation length $L_{\text{back}}^{\max}(|D|, F, \delta_{\min}, \delta_{\text{acc}})$ in Fig. 4.

APPENDIX F: MODES FOR HIGHEST PHOTON NUMBER RATES

The modes for maximal photon number rate $\Phi_{\text{L/R}}/\gamma_{\text{L/R}}^0$ are for a directionality $|D| = 0.99$ and minimal losses as a function of the Purcell enhancement F are highlighted in Fig. 11. The discreet sampling of the k-space allows only for discreet evaluation of the optimal mode with optical enhancement to loss-ratio. Particularly, for high enhancements involving high group indices, the finite sampling of the k-space limits the resolution of the optimal enhancement to loss ratio.

For increasing enhancement desired, the group index increases monotonously. When increasing the enhancements for the BIW the wave number k monotonously increases as well. For the BIW only modes of the upper band are optimal. In the case of the GPW the upper band shows less losses for the same group index compared to the lower band. However, the lower bands exceeds the upper bands maximal group index and thus its maximal accessible enhancement. Consequently, modes of the lower band with high losses are to be utilized above a certain desired Purcell enhancement.
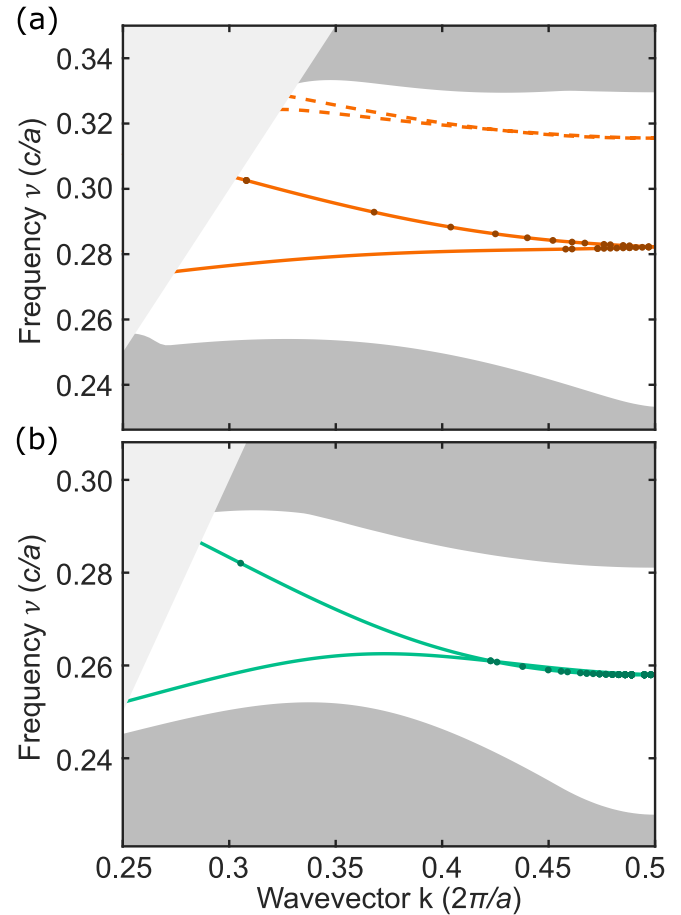

FIG. 11. Band diagram of the (a) GPW and (b) BIW showing only the light cone, the bulk bands, and the relevant modes for which the photon number rate $\Phi_{\text{L/R}}/\gamma_{\text{L/R}}^0$ is maximal, desiring a directionality of $|D| = 0.99$ and minimal losses. Each point shown corresponds to a different optimal Purcell enhancement.

[1] F. J. Rodríguez-Fortuño, G. Marino, P. Ginzburg, D. O'Connor, A. Martínez, G. A. Wurtz, and A. V. Zayats, Near-field interference for the unidirectional excitation of electromagnetic guided modes, Science **340**, 328 (2013).

[2] J. Lin, J. B. Müller, Q. Wang, G. Yuan, N. Antoniou, X.-C. Yuan, and F. Capasso, Polarization-controlled tunable directional coupling of surface plasmon polaritons, Science **340**, 331 (2013).

[3] J. Petersen, J. Volz, and A. Rauschenbeutel, Chiral nanophotonic waveguide interface based on spin-orbit interaction of light, Science **346**, 67 (2014).

[4] R. J. Coles, D. M. Price, B. Royall, E. Clarke, M. S. Skolnick, A. M. Fox, and M. Makhonin, Path-dependent initialization of a single quantum dot exciton spin in a nanophotonic waveguide, Phys. Rev. B **95**, 121401(R) (2017).

[5] P. Schneeweiss, S. Zeiger, T. Hoinkes, A. Rauschenbeutel, and J. Volz, Fiber ring resonator with a nanofiber section for chiral cavity quantum electrodynamics and multimode strong coupling, Opt. Lett. **42**, 85 (2017).

[6] D. Martin-Cano, H. R. Haakh, and N. Rotenberg, Chiral emission into nanophotonic resonators, ACS Photonics **6**, 961 (2019).

[7] B. Le Feber, N. Rotenberg, and L. Kuipers, Nanophotonic control of circular dipole emission, Nat. Commun. **6**, 6695 (2015).

[8] I. Söllner, S. Mahmoodian, S. L. Hansen, L. Midolo, A. Javadi, G. Kiršanskė, T. Pregnolato, H. El-Ella, E. H. Lee, J. D. Song *et al.*, Deterministic photon–emitter coupling in chiral photonic circuits, Nat. Nanotechnol. **10**, 775 (2015).

[9] A. B. Young, A. C. T. Thijssen, D. M. Beggs, P. Androvitsaneas, L. Kuipers, J. G. Rarity, S. Hughes, and R. Oulton, Polarization Engineering in Photonic Crystal Waveguides for Spin-Photon Entanglers, Phys. Rev. Lett. **115**, 153901 (2015).

[10] P. Lodahl, S. Mahmoodian, and S. Stobbe, Interfacing single photons and single quantum dots with photonic nanostructures, Rev. Mod. Phys. **87**, 347 (2015).

[11] K. Xia, G. Lu, G. Lin, Y. Cheng, Y. Niu, S. Gong, and J. Twamley, Reversible nonmagnetic single-photon isolation

using unbalanced quantum coupling, Phys. Rev. A **90**, 043802 (2014).

[12] C. Sayrin, C. Junge, R. Mitsch, B. Albrecht, D. O'Shea, P. Schneeweiss, J. Volz, and A. Rauschenbeutel, Nanophotonic Optical Isolator Controlled by the Internal State of Cold Atoms, Phys. Rev. X **5**, 041036 (2015).

[13] M. Scheucher, A. Hilico, E. Will, J. Volz, and A. Rauschenbeutel, Quantum optical circulator controlled by a single chirally coupled atom, Science **354**, 1577 (2016).

[14] I. Shomroni, S. Rosenblum, Y. Lovsky, O. Bechler, G. Guendelman, and B. Dayan, All-optical routing of single photons by a one-atom switch controlled by a single photon, Science **345**, 903 (2014).

[15] F. T. Pedersen, E. M. González-Ruiz, N. Hauff, Y. Wang, A. D. Wieck, A. Ludwig, R. Schott, L. Midolo, A. S. Sørensen, R. Uppu *et al.*, On-demand source of dual-rail photon pairs based on chiral interaction in a nanophotonic waveguide, arXiv:2109.03519.

[16] S. Mahmoodian, P. Lodahl, and A. S. Sørensen, Quantum Networks with Chiral-Light-Matter Interaction in Waveguides, Phys. Rev. Lett. **117**, 240501 (2016).

[17] A. B. Khanikaev, S. H. Mousavi, W.-K. Tse, M. Kargarian, A. H. MacDonald, and G. Shvets, Photonic topological insulators, Nat. Mater. **12**, 233 (2013).

[18] S. Raghu and F. D. M. Haldane, Analogs of quantum-Hall-effect edge states in photonic crystals, Phys. Rev. A **78**, 033834 (2008).

[19] T. Ma and G. Shvets, All-Si valley-Hall photonic topological insulator, New J. Phys. **18**, 025012 (2016).

[20] M. Hafezi, E. A. Demler, M. D. Lukin, and J. M. Taylor, Robust optical delay lines with topological protection, Nat. Phys. **7**, 907 (2011).

[21] Z. Wang, Y. Chong, J. D. Joannopoulos, and M. Soljac, Observation of unidirectional backscattering-immune topological electromagnetic states, Nature (London) **461**, 772 (2009).

[22] F. D. M. Haldane and S. Raghu, Possible Realization of Directional Optical Waveguides in Photonic Crystals with Broken Time-Reversal Symmetry, Phys. Rev. Lett. **100**, 013904 (2008).

[23] S. A. Skirlo, L. Lu, and M. Soljacic, Multimode One-Way Waveguides of Large Chern Numbers, Phys. Rev. Lett. **113**, 113904 (2014).

[24] M. J. Mehrabad, A. P. Foster, R. Dost, E. Clarke, P. K. Patil, A. M. Fox, M. S. Skolnick, and L. R. Wilson, Chiral topological photonics with an embedded quantum emitter, Optica **7**, 1690 (2020).

[25] T. Yamaguchi, Y. Ota, R. Katsumi, K. Watanabe, S. Ishida, A. Osada, Y. Arakawa, and S. Iwamoto, GaAs valley photonic crystal waveguide with light-emitting InAs quantum dots, Appl. Phys. Express **12**, 062005 (2019).

[26] S. Barik, A. Karasahin, C. Flower, T. Cai, H. Miyake, W. DeGottardi, M. Hafezi, and E. Waks, A topological quantum optics interface, Science **359**, 666 (2018).

[27] J. Li, R.-L. Chu, J. K. Jain, and S.-Q. Shen, Topological Anderson Insulator, Phys. Rev. Lett. **102**, 136806 (2009).

[28] X.-T. He, E.-T. Liang, J.-J. Yuan, H.-Y. Qiu, X.-D. Chen, F.-L. Zhao, and J.-W. Dong, A silicon-on-insulator slab for topological valley transport, Nat. Commun. **10**, 1 (2019).

[29] X.-L. Qi and S.-C. Zhang, Topological insulators and superconductors, Rev. Mod. Phys. **83**, 1057 (2011).

[30] M. Z. Hasan and C. L. Kane, Colloquium: Topological insulators, Rev. Mod. Phys. **82**, 3045 (2010).

[31] K. Fang, Z. Yu, and S. Fan, Realizing effective magnetic field for photons by controlling the phase of dynamic modulation, Nat. Photonics **6**, 782 (2012).

[32] G. Arregui, J. Gomis-Bresco, C. M. Sotomayor-Torres, and P. D. Garcia, Quantifying the Robustness of Topological Slow Light, Phys. Rev. Lett. **126**, 027403 (2021).

[33] Y. Yang, H. Jiang, and Z. H. Hang, Topological valley transport in two-dimensional honeycomb photonic crystals, Sci. Rep. **8**, 1588 (2018).

[34] M. I. Shalaev, W. Walasik, A. Tsukernik, Y. Xu, and N. M. Litchinitser, Robust topologically protected transport in photonic crystals at telecommunication wavelengths, Nat. Nanotech. **14**, 31 (2019).

[35] M. I. Shalaev, W. Walasik, and N. M. Litchinitser, Optically tunable topological photonic crystal, Optica **6**, 839 (2019).

[36] A. Blanco-Redondo, B. Bell, D. Oren, B. J. Eggleton, and M. Segev, Topological protection of biphoton states, Science **362**, 568 (2018).

[37] J. Jin, X. Yin, L. Ni, M. Soljačić, B. Zhen, and C. Peng, Topologically enabled ultrahigh-q guided resonances robust to out-of-plane scattering, Nature (London) **574**, 501 (2019).

[38] L. Sapienza, H. Thyrrestrup, S. Stobbe, P. D. Garcia, S. Smolka, and P. Lodahl, Cavity quantum electrodynamics with Anderson-localized modes, Science **327**, 1352 (2010).

[39] T. Crane, O. J. Trojak, J. P. Vasco, S. Hughes, and L. Sapienza, Anderson localization of visible light on a nanophotonic chip, ACS Photonics **4**, 2274 (2017).

[40] J. P. Vasco and S. Hughes, Statistics of Anderson-localized modes in disordered photonic crystal slab waveguides, Phys. Rev. B **95**, 224202 (2017).

[41] N. Mann and S. Hughes, Soliton Pulse Propagation in the Presence of Disorder-Induced Multiple Scattering in Photonic Crystal Waveguides, Phys. Rev. Lett. **118**, 253901 (2017).

[42] C. Husko, M. Wulf, S. Lefrancois, S. Combrié, G. Lehoucq, A. De Rossi, B. J. Eggleton, and L. Kuipers, Free-carrier-induced soliton fission unveiled by *in situ* measurements in nanophotonic waveguides, Nat. Commun. **7**, 11332 (2016).

[43] S. Mahmoodian, K. Prindal-Nielsen, I. Söllner, S. Stobbe, and P. Lodahl, Engineering chiral light–matter interaction in photonic crystal waveguides with slow light, Opt. Mater. Express **7**, 43 (2017).

[44] M. Saba, S. Wong, M. Elman, S. S. Oh, and O. Hess, Nature of topological protection in photonic spin and valley-Hall insulators, Phys. Rev. B **101**, 054307 (2020).

[45] P. Lodahl, S. Mahmoodian, S. Stobbe, A. Rauschenbeutel, P. Schneeweiss, J. Volz, H. Pichler, and P. Zoller, Chiral quantum optics, Nature (London) **541**, 473 (2017).

[46] E. M. Purcell, Spontaneous emission probabilities at radio frequencies, in *Confined Electrons and Photons* (Springer, Berlin, 1995), pp. 839–839.

[47] S. Hughes, Enhanced single-photon emission from quantum dots in photonic crystal waveguides and nanocavities, Opt. Lett. **29**, 2659 (2004).

[48] S. Schulz, L. O'Faolain, D. M. Beggs, T. P. White, A. Melloni, and T. F. Krauss, Dispersion engineered slow light in photonic crystals: A comparison, J. Opt. **12**, 104004 (2010).

[49] M. Arcari, I. Söllner, A. Javadi, S. Lindskov Hansen, S. Mahmoodian, J. Liu, H. Thyrrestrup, E. H. Lee, J. D. Song,

S. Stobbe, and P. Lodahl, Near-Unity Coupling Efficiency of a Quantum Emitter to a Photonic Crystal Waveguide, Phys. Rev. Lett. **113**, 093603 (2014).

[50] S. Hughes, L. Ramunno, J. F. Young, and J. E. Sipe, Extrinsic Optical Scattering Loss in Photonic Crystal Waveguides: Role of Fabrication Disorder and Photon Group Velocity, Phys. Rev. Lett. **94**, 033903 (2005).

[51] J. D. Joannopoulos, P. R. Villeneuve, and S. Fan, Photonic crystals, Solid State Commun. **102**, 165 (1997).

[52] E. Sauer, J. P. Vasco, and S. Hughes, Theory of intrinsic propagation losses in topological edge states of planar photonic crystals, Phys. Rev. Research **2**, 043109 (2020).

[53] Z. F. Ezawa, *Quantum Hall Effects: Field Theoretical Approach and Related Topics* (World Scientific, Singapore, 2008).

[54] S. Arora, T. Bauer, R. Barczyk, E. Verhagen, and L. Kuipers, Direct quantification of topological protection in symmetry-protected photonic edge states at telecom wavelengths, Light Sci. Appl. **10**, 9 (2021).

[55] Y. Plotnik, M. C. Rechtsman, D. Song, M. Heinrich, J. M. Zeuner, S. Nolte, Y. Lumer, N. Malkova, J. Xu, A. Szameit *et al.*, Observation of unconventional edge states in "photonic graphene," Nat. Mater. **13**, 57 (2014).

[56] E. Kuramochi, M. Notomi, S. Hughes, A. Shinya, T. Watanabe, and L. Ramunno, Disorder-induced scattering loss of line-defect waveguides in photonic crystal slabs, Phys. Rev. B **72**, 161318(R) (2005).

[57] N. Mann, A. Javadi, P. D. García, P. Lodahl, and S. Hughes, Theory and experiments of disorder-induced resonance shifts and mode-edge broadening in deliberately disordered photonic crystal waveguides, Phys. Rev. A **92**, 023849 (2015).

[58] V. S. C. Manga Rao and S. Hughes, Single Quantum Dot Spontaneous Emission in a Finite-Size Photonic Crystal Waveguide: Proposal for an Efficient "on chip" Single Photon Gun, Phys. Rev. Lett. **99**, 193901 (2007).

[59] M. Patterson, S. Hughes, S. Schulz, D. M. Beggs, T. P. White, L. O'Faolain, and T. F. Krauss, Disorder-induced incoherent scattering losses in photonic crystal waveguides: Bloch mode reshaping, multiple scattering, and breakdown of the Beer-lambert law, Phys. Rev. B **80**, 195305 (2009).

[60] Adapted from Ref. [88] for nonuniform hole sizes R_α.

[61] A. Parini, P. Hamel, A. De Rossi, S. Combrié, N.-V.-Q. Tran, Y. Gottesman, R. Gabet, A. Talneau, Y. Jaouen, and G. Vadala, Time-wavelength reflectance maps of photonic crystal waveguides: A new view on disorder-induced scattering, J. Lightwave Technol. **26**, 3794 (2008).

[62] M. Skorobogatiy, G. Bégin, and A. Talneau, Statistical analysis of geometrical imperfections from the images of 2D photonic crystals, Opt. Express **13**, 2487 (2005).

[63] B. Gmeiner, A. Maser, T. Utikal, S. Götzinger, and V. Sandoghdar, Spectroscopy and microscopy of single molecules in nanoscopic channels: Spectral behavior vs. confinement depth, Phys. Chem. Chem. Phys. **18**, 19588 (2016).

[64] S. Liu, K. Srinivasan, and J. Liu, Nanoscale positioning approaches for integrating single solid-state quantum emitters with photonic nanostructures, Laser Photonics Rev. **15**, 2100223 (2021).

[65] Y. Romach, C. Muller, T. Unden, L. J. Rogers, T. Isoda, K. M. Itoh, M. Markham, A. Stacey, J. Meijer, S. Pezzagna, B. Naydenov, L. P. McGuinness, N. Bar-Gill, and F. Jelezko,

Spectroscopy of Surface-Induced Noise Using Shallow Spins in Diamond, Phys. Rev. Lett. **114**, 017601 (2015).

[66] P. Schnauber, J. Schall, S. Bounouar, T. Höhne, S.-I. Park, G.-H. Ryu, T. Heindel, S. Burger, J.-D. Song, S. Rodt *et al.*, Deterministic integration of quantum dots into on-chip multimode interference beamsplitters using *in situ* electron beam lithography, Nano Lett. **18**, 2336 (2018).

[67] M. Gschrey, R. Schmidt, J.-H. Schulze, A. Strittmatter, S. Rodt, and S. Reitzenstein, Resolution and alignment accuracy of low-temperature *in situ* electron beam lithography for nanophotonic device fabrication, J. Vac. Sci. Technol. B **33**, 021603 (2015).

[68] T. Pregnolato, X.-L. Chu, T. Schröder, R. Schott, A. D. Wieck, A. Ludwig, P. Lodahl, and N. Rotenberg, Deterministic positioning of nanophotonic waveguides around single self-assembled quantum dots, APL Photon. **5**, 086101 (2020).

[69] In all-dielectric media light propagation is described by Maxwell's equations obeying time-reversal symmetry. In that regard the overall performance of the discussed chiral interfaces for a given diretionality D is identical to a directionlity $-D$.

[70] For photonic crystals there is no fundamental constant with the dimension of length since the master equation in dielectric media is scale invariant. A quantum emitter can be brought in resonance with a mode of wave number k by scaling the lattice constant a.

[71] M. Patterson, S. Hughes, S. Combrié, N.-V.-Quynh Tran, A. De Rossi, R. Gabet, and Y. Jaouën, Disorder-Induced Coherent Scattering in Slow-Light Photonic Crystal Waveguides, Phys. Rev. Lett. **102**, 253903 (2009).

[72] M. Jalali Mehrabad, A. Foster, R. Dost, E. Clarke, P. Patil, I. Farrer, J. Heffernan, M. Skolnick, and L. Wilson, A semiconductor topological photonic ring resonator, Appl. Phys. Lett. **116**, 061102 (2020).

[73] S. Barik, A. Karasahin, S. Mittal, E. Waks, and M. Hafezi, Chiral quantum optics using a topological resonator, Phys. Rev. B **101**, 205303 (2020).

[74] M. C. Rechtsman, J. M. Zeuner, Y. Plotnik, Y. Lumer, D. Podolsky, F. Dreisow, S. Nolte, M. Segev, and A. Szameit, Photonic floquet topological insulators, Nature (London) **496**, 196 (2013).

[75] D. E. Chang, V. Vuletić, and M. D. Lukin, Quantum nonlinear optics-photon by photon, Nat. Photonics **8**, 685 (2014).

[76] T. Volz, A. Reinhard, M. Winger, A. Badolato, K. J. Hennessy, E. L. Hu, and A. Imamoğlu, Ultrafast all-optical switching by single photons, Nat. Photonics **6**, 605 (2012).

[77] A. Javadi, I. Söllner, M. Arcari, S. L. Hansen, L. Midolo, S. Mahmoodian, G. Kiršanskė, T. Pregnolato, E. Lee, J. Song *et al.*, Single-photon nonlinear optics with a quantum dot in a waveguide, Nat. Commun. **6**, 8655 (2015).

[78] K. Koshino, S. Ishizaka, and Y. Nakamura, Deterministic photon-photon swap gate using a λ system, Phys. Rev. A **82**, 010301(R) (2010).

[79] E. Nussbaum, E. Sauer, and S. Hughes, Inverse design of broadband and lossless topological photonic crystal waveguide modes, Opt. Lett. **46**, 1732 (2021).

[80] R. E. Christiansen, F. Wang, O. Sigmund, and S. Stobbe, Designing photonic topological insulators with quantum-spin-Hall edge states using topology optimization, Nanophotonics **8**, 1363 (2019).

[81] J. S. Jensen and O. Sigmund, Topology optimization for nano-photonics, Laser Photonics Rev. **5**, 308 (2011).

[82] N. Mann, S. Combrié, P. Colman, M. Patterson, A. De Rossi, and S. Hughes, Reducing disorder-induced losses for slow light photonic crystal waveguides through Bloch mode engineering, Opt. Lett. **38**, 4244 (2013).

[83] T. Baba and D. Mori, Slow light engineering in photonic crystals, J. Phys. D **40**, 2659 (2007).

[84] Y. Chen, F. Meng, Y. Kivshar, B. Jia, and X. Huang, Inverse design of higher-order photonic topological insulators, Phys. Rev. Research **2**, 023115 (2020).

[85] S. Adachi, GaAs, AlAs, and $Al_xGa_{1x}As$: Material parameters for use in research and device applications, J. Appl. Phys. **58**, R1 (1985).

[86] J. D. Joannopoulos, S. G. Johnson, J. N. Winn, and R. D. Meade, *Molding the Flow of Light* (Princeton University Press, Princeton, NJ, 2008).

[87] B. Wang, S. Mazoyer, J.-P. Hugonin, and P. Lalanne, Backscattering in monomode periodic waveguides, Phys. Rev. B **78**, 245108 (2008).

[88] M. Patterson and S. Hughes, Interplay between disorder-induced scattering and local field effects in photonic crystal waveguides, Phys. Rev. B **81**, 245321 (2010).